Void nucleation and disentanglement in glassy amorphous polymers

Dhiraj K. Mahajan, Bhupinder Singh, and Sumit Basu*
Department of Mechanical Engineering, Indian Institute of Technology Kanpur, Kanpur 208016, UP, India
(Received 26 January 2010; revised manuscript received 29 April 2010; published 27 July 2010)

Cavitation in glassy polymers is known to result from highly triaxial states of local stress and the presence of impurities. Understanding of cavitation, particularly void nucleation, is important as cavities are precursors to crazes, which in turn lead to fracture. In this work we study the early stages of void nucleation in glassy amorphous polymers by imposing, in well designed molecular dynamics simulations, highly triaxial states of stress on ensembles of entangled linear macromolecular chains and monitoring the evolution of the entanglement network. Our results demonstrate that deformation induced disentanglement and rearrangement of topological constraints along individual chains play an important role in the early stages of void nucleation. Even in the glassy state, deformation causes significant changes in the rheological constraints on a chain though the number of interchain binary contacts may not change much.

DOI: 10.1103/PhysRevE.82.011803 PACS number(s): 82.35.Lr, 83.50.−v, 81.05.Lg, 66.70.Hk

I. INTRODUCTION

Crazing is an important failure mechanism in glassy polymers which involves the formation of crack-like defects bridged by numerous thin stress carrying fibrils. Crazes are known to nucleate at locations where the hydrostatic stress is high. Though it is not clear if the presence of high hydrostatic stress is sufficient for nucleation, craze initiation criteria have been proposed (see, e.g., [1]) that imply impossibility of crazing under deviatoric stress states. The importance of the hydrostatic stress state stems from the fact that craze nucleation is preceded by cavitation [2], which in turn is aided by the presence of embedded dust particles or other impurities [3].

There are a number of views on how the first cavities come about in an amorphous polymer well below its glass transition temperature T_g. According to Argon [3], crazes nucleate when a critical amount of porosity is attained in thermally activated shear patches which cavitate when their ends are blocked. Gent [4] conjectured that the locally high hydrostatic stress levels close to a crack or flaw leads to a local diminution in T_g causing the material to turn rubbery and hence more prone to cavitation. Dettenmaier and Kausch [5] and Dettenmaier [6] proposed a mechanism of crazing that operates through stress-induced disentanglement of chains at high levels of strain and temperatures close to but below T_g.

As has been amply demonstrated by Kramer and coworkers (see, e.g., [7]), the extension ratios of crazes in a particular polymer are correlated with the maximum extension ratio of a strand between two entanglement points. This implies that the underlying entanglement network formed by the macromolecules plays a very significant role in craze widening. However, the role of the entanglement network in the early stages of cavitation that precedes craze growth has not been adequately discussed in the literature.

In this paper we study the micromechanics of the very early stages of cavitation in glassy polymers through molecular dynamics (MD) simulations. In particular, we subject ensembles of entangled macromolecules to a combination of high hydrostatic stresses superposed on uniaxial tension. The imposed triaxial state of stress promotes cavitation and simultaneously, we follow the evolution of the entanglement network with deformation. Recent developments [8–11] allow us to quantitatively estimate various parameters pertaining to the entanglement network, especially the entanglement length N_e. Careful characterization of the entanglement network at various levels of deformation reveal that deformation induced disentanglement of chains occur in the glassy regime and indeed, cavitation in glassy polymers is an outcome of both disentanglement and rearrangement of entanglement points during deformation. The consequences of this finding are discussed in detail.

The paper is organized in the following manner. In the next section we briefly outline the force fields used for our MD simulations and the methods of sample generation employed. The various techniques adopted for characterizing entanglement networks are detailed and discussed in Sec. III. Important results from our analyses and discussions on them are presented in Sec. IV while the salient conclusions are enumerated in Sec. V

II. COMPUTATIONAL PROCEDURE

In this section we will briefly describe the force field and generation techniques adopted for ensembles of linear macromolecular chains. The reader is referred to Mahajan and Basu [12] for a more detailed account. It should be noted that generation of reliable glassy samples of macromolecules starts from generation of a sample at a temperature well above T_g that is well equilibrated at short and long length scales. This sample is then quenched slowly to a temperature below T_g. The extent to which short and long range equilibration is achieved above T_g, rates of quenching, sample size, and the rate of deformation at the glassy temperature all play important roles in determining the deformation behavior of the glassy sample. These issues have been discussed in detail in Mahajan and Basu [13].

*http://home.iitk.ac.in/-sbasu; sbasu@iitk.ac.in

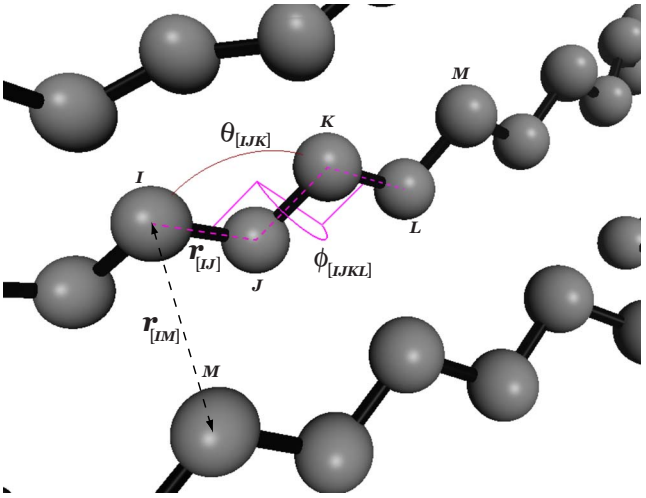

FIG. 1. (Color online) Schematic explaining the notation used in Eq. (1).

In this work we use a detailed atomistic model of a polymer for which the total internal energy is given by,

$$\mathcal{U} = \sum_{[IJ]=1}^{n_b} U_b(r_{[IJ]}) + \sum_{[IJK]=1}^{n_\theta} U_\theta(\theta_{[IJK]}) + \sum_{[IJKL]=1}^{n_\phi} U_\phi(\phi_{[IJKL]}) + \sum_{[IM]=1}^{n_{vdW}} U_{vdW}(r_{[IM]}). \quad (1)$$

The atom numbering used in the above equation is also shown in Fig. 1. We use the notation $[IJ\ldots]$ to denote the index of a group of atoms $I,J,\ldots$ forming a bond. Thus $[IJ]$ denotes the index of a particular intrachain bond that connects atoms I and J while r_{IJ} is the distance between them. Similarly n_θ and n_ϕ denote the number of bond and dihedral angles while $[IJK]$ and $[IJKL]$ are indices labeling particular instances of interacting, bonded atom groups. The number of nonbonded pairs is denoted by n_{vdW} where M and I can be in located on different chains or be a non bonded pair on the same chain.

Though we do not intend to simulate a particular polymer, the force field parameters chosen closely resemble those for polyethylene (PE) (see, [14]]) and atoms within a chain have masses equivalent to CH_2 while end atoms have masses corresponding to CH_3. Polyethylene is the simplest detailed macromolecular system and has been studied for its mechanical properties by several authors (e.g., [15–17], among others). In principle, any macromolecule can be coarse grained into a PE-like system with a different set of force field parameters (see, [18–21], for examples of such efforts).

Furthermore, we use uppercase Roman letters for atom indices and Greek superscripts for vector or tensor components. Using this convention and the notation introduced in Fig. 1, the force field consists of

(1) A harmonic bond stretching potential between any two consecutive atoms I and J in a chain of the form:

$$U_b(r_{[IJ]}) = \frac{1}{2}k_b(r_{[IJ]} - r_0)^2, \quad (2)$$

where r_0 is the equilibrium bond length and k_b is the bond stiffness. In this work, we choose $k_b = 2745$ kJ Å^{-2} mol^{-1} and $r_o = 1.53$ Å for all bonds.

(2) A bond bending potential, also assumed to be harmonic, with an equilibrium bond angle θ_0 defined as

$$U_\theta[\theta_{(IJK)}] = \frac{1}{2}k_\theta\{\cos[\theta_{(IJK)}] - \cos(\theta_0)\}^2, \quad (3)$$

where $k_\theta = 749$ kJ mol^{-1} and $\theta_0 = 113.3°$.

(3) A torsion potential of the form,

$$U_\phi[\phi_{(IJKL)}] = \frac{1}{2}A_1\{1 + \cos[\phi_{(IJKL)}]\} + \frac{1}{2}A_2\{1 - \cos[2\phi_{(IJKL)}]\} + \frac{1}{2}A_3\{1 + \cos[3\phi_{(IJKL)}]\}, \quad (4)$$

with $A_1 = 7.86$, $A_2 = -4.36$, and $A_3 = 15.56$ kJ mol^{-1} being used in this work.

(4) A nonbonded Lenard Jones (LJ) potential of the form:

$$U_{vdW}(r_{[IM]}) = 4\epsilon\left[\left(\frac{\sigma}{r_{[IM]}}\right)^{12} - \left(\frac{\sigma}{r_{[IM]}}\right)^{6}\right]. \quad (5)$$

In the LJ equation, $\sigma = 3.76$ Å and $\epsilon = 0.88$ kJ mol^{-1} between end atoms while $\sigma = 4.06$ Å and $\epsilon = 0.36$ kJ mol^{-1} between all other nonbonded atoms. In all calculations, a van der Waals cutoff radius r_c of 6 Å is used.

All NVT simulations are performed using a Nose-Hoover thermostat with time constant $\tau_T = 0.5$ ps while NPT simulations additionally use a Nose-Hoover barostat with the time constant $\tau_P = \tau_T$. Integration of the Newtonian equations of motion are performed with the leapfrog variant of the velocity Verlet algorithm with a typical time step of $\Delta t = 2$ fs. Periodic boundary conditions are used in all analyses reported. The various macromolecular samples studied in this work have chain lengths N of 200, 500, and 1000, with total number of monomers as 32000.

The procedure adopted for generating macromolecular samples closely resembles that described by Auhl *et al.* [22]. This method attempts to control the configurational statistics of the ensembles generated with a view to producing well equilibrated internal structures at long and short length scales. The protocol for generating the ensembles involves a number of steps which are detailed in Mahajan and Basu [12]. Following these steps, well equilibrated ensembles with $N = 200$, 500, and 1000 atoms were created. As discussed in Auhl *et al.* [22], equilibration of samples with $N > 200$ is especially difficult. The quality of the equilibration is judged on several counts. Constancy of the total system energy, volume, pressure, and temperature over time, equilibration of the structure at small length scales (i.e., attainment of sharply peaked distributions for bond lengths, angles and dihedrals with the peaks coinciding with the minimum energy locations in U_b, U_θ, and U_ϕ) are some of the most basic criteria. Additionally, the variation of end to end distance $\langle R^2(n)\rangle$ (calculated on chain segments of size n, $n \in [1,N]$), is expected to attain a constant value of C_∞ at large n, irrespective

of the chain length N. We have already demonstrated in Mahajan and Basu [12] that all our samples fulfill this requirement and attain a C_∞ of slightly above 7.

After the samples at 400 K are equilibrated, they are quenched to 100 K at 1.5 K/ps (which amounts to a decrease of 0.003 K per MD step). The samples undergo a glass transition close to $T_g \simeq 230$ K (the exact value of T_g is weakly dependent on the chain length at least in the range of cooling rates used in this work) and glassy samples are obtained at 100 K. It should be noted that the quenching rate used has an effect on the stress strain response [13] that we seek to obtain. This assumes importance in studies of aging (as will be demonstrated in a forthcoming paper) and should not concern us here. However, interestingly, recent Monte Carlo simulations on amorphous PE by Alexiadis *et al.* [23] yield $T_g = 230 \pm 10$ K which, in turn is close to the experimentally observed value of 237 K [24] in the limit of zero crystallinity.

The periodic boxes quenched to glassy temperature of 100 K are subjected to deformations where the stretch rates $\dot{\lambda}$ are controlled to be of the form

$$\dot{\lambda}^z = \dot{\lambda} \quad \text{and}$$

$$\dot{\lambda}^x = \dot{\lambda}^y = 0, \tag{6}$$

where,

$$\dot{\lambda} = \frac{\lambda_0}{t_r}\mathcal{H}(t_r - t). \tag{7}$$

In the above equation, $\mathcal{H}(x)$ is the Heaviside function which is unity for positive x and zero otherwise. The principal stretch in the 3 direction is λ which is ramped up to λ_0 in a time t_r. Note that as λ^x and λ^y are kept fixed at zero, the periodic box is not allowed to contract in the transverse direction. This creates a state of stress with a large triaxial part and hence promotes cavitation.

The glassy samples at 100 K are strained such that the total time of the simulation is t_r which means that the Heaviside function is unity all through the simulation. This involves increasing the periodic cell dimension at every MD step in the 3 direction at a rate of 50 m/s leading to an approximate strain rate of 5×10^{-3} ps^{-1}.

III. CHARACTERIZATION OF THE ENTANGLEMENT NETWORK

Typical experimental estimates of the entanglement length N_e, are based on the plateau modulus G_N^0 as

$$N_e = \frac{4}{5}\frac{\eta k_B T}{G_N^0}, \tag{8}$$

where, k_B denotes the Boltzmann constant, $\eta = \rho / M_0$, ρ being the density of the polymer and M_0 the weight of a monomer. The entanglement length can also be estimated by reducing all macromolecular chains in an ensemble to their primitive paths (PP). Primitive path is the shortest path a chain fixed at its ends can follow without crossing any other chain in the ensemble. Computational techniques for the reduction of an ensemble of macromolecules to a network of PPs has been accomplished by Sukumaran *et al.* [8], Kroger [9], Tzoumanekas and Theodorou [11], Everaers *et al.* [25], Shanbhag and Larson [26]. A brief description of the technique used by us is in place here and is presented below.

We closely follow the method outlined by Sukumaran *et al.* [8], adapted to the force field used in this work. The process involves the following steps:

(1) Samples with $N = 200$ to 1000, equilibrated in the manner and using the force field described above, are chosen.

(2) In an ensemble, the end points of all chains are fixed so that the end to end distances remain unchanged through the subsequent processes.

(3) All *intrachain* nonbonded interactions as well as the dihedral and angular potentials [Eqs. (3) and (4)] are turned off.

(4) The equilibrium bond length r_0 [Eq. (2)] and the temperature are slowly reduced to zero. In our case, we reduced the bond length r_0 from 1.53 to 0.05 Å while the final temperature attained was 10 K. The re-equilibriation to 10 K was achieved in about 100 $000\Delta t$, where Δt denotes the time step used. Note that the gradual reduction of r_0 is necessitated by the fact that we use a bond stretching potential that has a minimum at a nonzero length, unlike Sukumaran *et al.* [8].

As the chain ends are held fixed, attempts to equilibrate the system to a small r_0 results in all chains being pulled taut. At the same time, the *interchain* nonbonded interactions prevent the chains from crossing each other, finally producing a network of PPs. It was verified that for all the chain lengths used, lowering r_0 below 0.05 Å did not change the average bond length to any significant degree. Also, at $r_0 = 0.05$ Å and $T = 10$ K, all bond angles and dihedrals cluster around 180°.

After obtaining the PPs, the entanglement length is determined using the relation

$$N_e^{\text{rheo}} = (N-1)\frac{\langle R_{ee}^2 \rangle}{\langle L_{pp} \rangle^2}, \tag{9}$$

where, R_{ee} is the end to end distance and L_{pp} the contour length of the PP of a chain, while $\langle\ \rangle$ denotes an average over the ensemble. The above relation assumes that the PPs are, on an average, random walks with step lengths equal to N_e^{rheo}. The superscript to the value of N_e is justified by the fact that the entanglement length obtained by the above formula agrees well with rheological measures derived from Eq. (8) for long chains.

In a previous paper Mahajan and Basu [12], we have used the force field described in Sec. II and Eq. (8) to calculate N_e for N ranging from 90 to 1000 at 400 K. Though this method is prone to large margins of error especially at short chain lengths, the value of N_e^{rheo}, at large N, attains a length independent value of about $40(\pm 3)$. The Eq. (9) yields a N_e^{rheo} of 43 at $N = 1000$. In fact, values of entanglement length obtained from Eq. (9) at all N, match those obtained from the plateau modulus quite closely.

An alternative to Eq. (9) is provided by approaches where N_e is derived by directly 'counting' the number of internal

TABLE I. Comparison between the values of entanglement length obtained by various methods.

N	200		500		1000	
Temperature	100 K	400 K	100 K	400 K	100 K	400 K
From Eq. (8)		70 ± 15		42 ± 7		40 ± 3
From Eq. (9)	47	48	41	43	41	43
From Eq. (10)	23	23	20	21	20	20

kinks Q on every chain in a network of PPs. These kinks are identified as contacts between PPs (see, e.g., [9,11,26,27]). As pointed out by Hoy *et al.* [10], these methods yield the average number of entanglements per chain $\langle Q \rangle$. To obtain N_e we will use the simple estimator,

$$N_e^{\text{topo}} = \frac{N}{\langle Q \rangle}, \tag{10}$$

proposed by Hoy *et al.* [10]. The values of entanglement length for various chain lengths and obtained by Eqs. (8)–(10) are listed in Table I. Note that while the values of entanglement length obtained by Eqs. (9) and (8) are close to each other [the values from Eq. (9) and (8) are close for $N \geq 500$], the value of N_e^{topo} are much lower.

Hoy *et al.* [10] discusses the need for and merits of several improved estimators for entanglement length. Geometrical methods to enumerate the number of entanglements include schemes like CReTA [11] and Z1 [9]. The Z1 code due to Kroger [9] uses a set of geometric operations to simultaneously reduce the length of all chains and keep track of potentially intersecting segments. The code carries on the iterations over all chains in an ensemble till no more changes to the Euclidean lengths of the chains are possible. The outcome of the code is the number of "kinks" Q on every chain and hence the average $\langle Q \rangle$.

As already noted, Eq. (9) yields a value of N_e^{rheo} which is typically higher than that obtained from direct enumeration methods like N_e^{topo} by a factor of about 2–2.5. Tzoumanekas and Theodorou [11] discusses this discrepancy at length. As estimates from Eqs. (8) and (9) agree quite well, it is reasonable to assume that N_e^{rheo} is related to the number of effective entanglements along a chain that restrict its motion. However, each rheological entanglement, on an average, is constituted of 2–2.5 topological constraints which simply are binary contacts between PPs and show up as kinks on it. A binary contact between two chains (which is what is counted by N_e^{topo} is not enough to act as a strong enough constraint to restrict the motion of the chains. Several such closely spaced binary contacts may be needed to act as sufficient constraint to the chain's motion. These group of binary contacts will act as one constraining point and their numbers are counted by N_e^{rheo}. Loosely speaking, in order to affect a constraint on the motion of a chain it is necessary to have multiple binary topological contacts and hence, interactions with a large number of neighboring chains. The distinction between N_e^{rheo} and N_e^{topo} will have important bearing on the interpretation of results to be discussed in the following.

IV. RESULTS AND DISCUSSIONS

We are primarily interested in the evolution of the entanglement length with deformation of a polymer in the glassy state. To this end, we first quench a sample prepared at 400 K to a glassy temperature of 100 K. The glassy sample is then subjected to a triaxial state of stress as given by Eq. (6) which is conducive to the nucleation of voids. At different stages of the deformation λ, we perform PP analyses in the manner described in the previous section to determine N_e^{rheo}. Further, N_e^{topo} is obtained at the same value of λ by using the Z1 code [9] and Eq. (10).

Figure 2 shows the values of both rheological and topological values of entanglement length obtained from a sample with $N=500$ at various levels of λ. Primitive Path analyses have been conducted at intervals of 10% strain in both cases. At $\lambda=1$, the glassy sample has almost the same value of $N_e^{\text{rheo}} \simeq 45$ as the sample at 400 K, indicating that the entanglement network existing above T_g remains intact and simply freezes into the glassy state as the sample is quenched. This is also evident from the values of entanglement length for various values of N listed in Table I.

However, N_e^{rheo} changes almost linearly with λ, attaining a

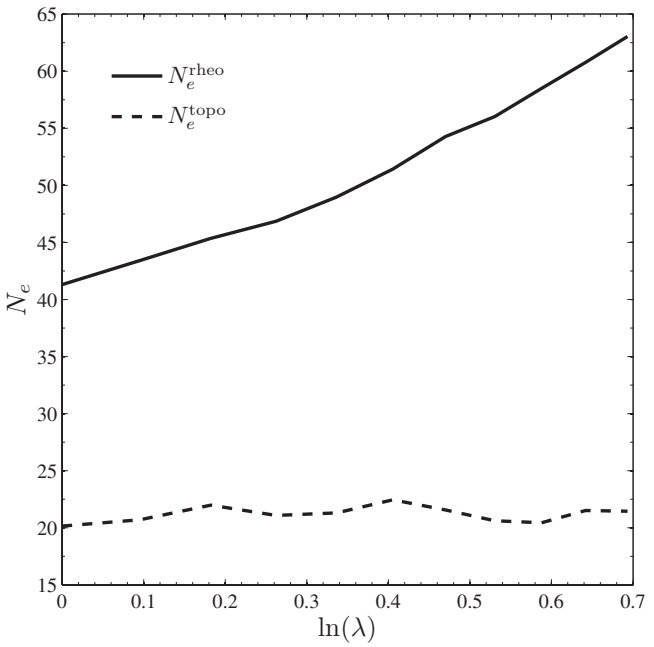

FIG. 2. Variation of N_e with uniaxial deformation, where N_e^{rheo} is based on Eq. (9), while N_e^{topo} is obtained from Eq. (10).

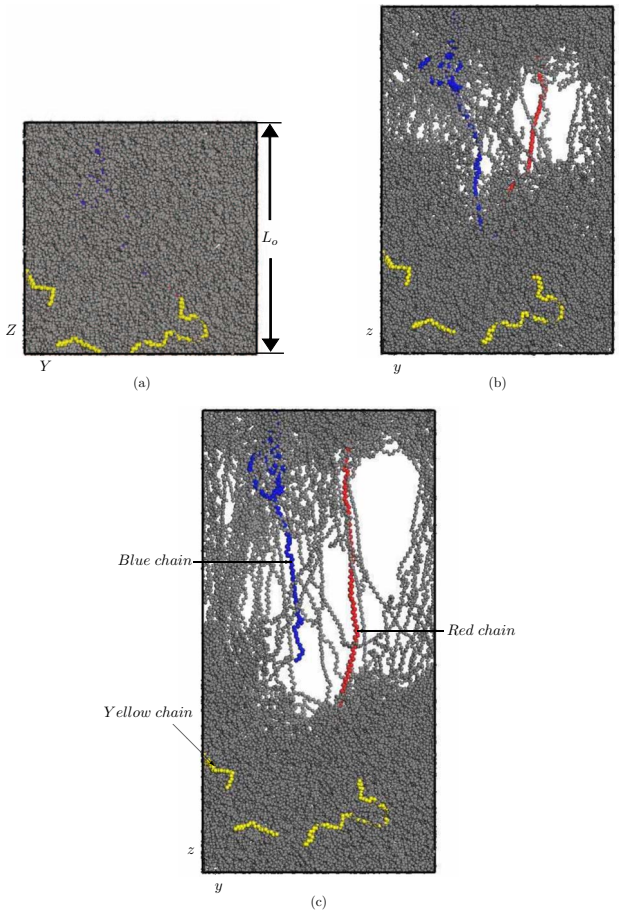

FIG. 3. (Color online) Deformed configuration at $\lambda=1.0$ (a), 1.5 (b), and 2.0 (c). Three chains are colored yellow, blue and red to facilitate reference in the text.

value of above 63 at $\lambda=2$, indicating a significant decrease in the density of entanglements. Interestingly, throughout the deformation history, N_e^{topo}, also shown in Fig. 2 and calculated at the same levels of λ, shows only a slight, almost imperceptible, increase. Thus, a rheological entanglement which was equivalent to about 2 topological ones at the start of the deformation, is related to about 3.1 topological entanglements at the end.

The above figure demonstrates that deformation induces loss of rheological entanglements. This is further illustrated by Figs. 3(a)–3(c), where deformed configurations of the initially cubic periodic simulation box is shown at $\lambda=1$, 1.5, and 2.0 for $N=200$. Clearly, the high triaxiality imposed by the deformation leads to the nucleation and growth of a voided region slightly above the center of the box. We have also identified three chains on the basis of their situation at $\lambda=2$ and have colored them differently. The yellow chain lies in the bulk at $\lambda=2$. The blue and red chains lie in the voided region but while one end of the blue chain has pulled out from the bulk at $\lambda=2$, the red chain is firmly anchored.

Further, in Fig. 4, we show the variation in the total number of kinks Q with height at the three values of λ. To obtain these curves, the entire height of the box has been divided into along the z-direction into ten slabs of equal thickness and the quantity Q in the abscissa denotes the number of kinks falling within each slab. Again, in spite of the noisy nature of the data, there is clearly a drop in the number of kinks or topological entanglements at the location of the emerging void. At the onset the number of kinks is uniformly distributed over the height of the sample. As the void develops, there is a drop in the number of kinks (implying that chain segments are becoming taut in this region) at the location of the void accompanied by an increase in nonvoided regions at the bottom of the box.

It should be noted at this point that, though the number of kinks at the location of the void is low, globally the number of kinks remains almost the same throughout the deformation history. To understand how this happens, we chose the three chains identified above and shown in Fig. 5. Shown schematically in Fig. 5 are the locations of the kinks along these chains at $\lambda=1$ and 2. For the chain that remains in the bulk all through the deformation, the kinks redistribute with deformation but long gaps do not open up. For a few suitably located "lucky" chains, the redistribution might lead to long gaps opening up either in the middle of the chain (e.g., the red chain) or chain ends (e.g., blue chain). If these gaps open up in the middle of the chain, the portion freed of entanglements and unhindered by interchain nonbonded interactions may uncoil and stretch while the ends remain firmly anchored. This will continue till either the ends pull out or the chain breaks. Gaps opening up at the ends cause the chain to pull out of the bulk as in the case of the lower end of the blue chain. Similar disentanglement behavior has been reported in case of reinforced polymer-substrate interfaces by Terzis *et al.* [28].

While some amount of redistribution of kinks happen for all chains in an ensemble (e.g., the yellow chain in the bulk), dramatic rearrangements are more localized (as in the voided part in Fig. 3). It is not clear why a particular location is favored for the rearrangement of kinks but localized chain slippage and void nucleation is definitely aided by triaxiality as similar events are not observed in incompressible deformations. At this stage it is not clear how a "lucky" chain is selected. It may be related to the fact that the local level of triaxiality is higher at the location of the chain or it is located in a region with a locally high concentration of chain ends.

For all the chains that have a part in the eventual location of the void, the scenario discussed above is true. With all the topological entanglements clustered at the ends of these chains, the effective rheological constraint on these chains is much weaker than on others. For example, for the red chain there are effectively two entanglements at its two ends while for the blue one, there is effectively one at the middle. We believe that such "lucky" chains cause the overall rheological entanglement density to drop and the consequent increase in N_e^{rheo} with deformation.

We have also calculated the stress components, particularly Σ^{zz}, based on various volume measures as shown by the curves in Fig. 6. The stress tensor $\Sigma^{\alpha\beta}(\alpha,\beta=x,y \text{ or } z)$ is calculated using the formula [29]

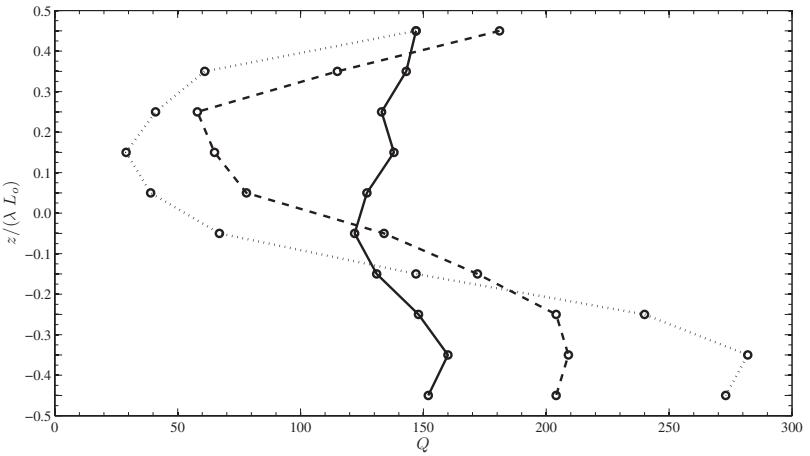

FIG. 4. Variation of total number of kinks Q in slabs of equal thickness along the z-direction with λ.

$$\Omega\Sigma^{\alpha\beta} = -\frac{1}{2}\sum_{[IM]=1}^{n_{vdW}} r^{\alpha}_{[IM]}\frac{\partial U_{vdW}(r_{[IM]})}{\partial r_{[IM]}}\frac{r^{\beta}_{[IM]}}{r_{[IM]}} - \sum_{[IJ]=1}^{n_b}\left\{ r^{\alpha}_{I}\frac{\partial U_b(r_{[IJ]})}{\partial r^{\beta}_{I}} + r^{\alpha}_{J}\frac{\partial U_b(r_{[IJ]})}{\partial r^{\beta}_{J}}\right\} - \sum_{[IJK]=1}^{n_\theta}\left\{ r^{\alpha}_{I}\frac{\partial U_\theta(\theta_{[IJK]})}{\partial r^{\beta}_{I}} + r^{\alpha}_{J}\frac{\partial U_\theta(\theta_{[IJK]})}{\partial r^{\beta}_{J}} + r^{\alpha}_{K}\frac{\partial U_\theta(\theta_{[IJK]})}{\partial r^{\beta}_{K}}\right\} - \sum_{[IJKL]=1}^{n_\phi}\left\{ r^{\alpha}_{I}\frac{\partial U_\phi(\phi_{[IJKL]})}{\partial r^{\beta}_{I}} + r^{\alpha}_{J}\frac{\partial U_\phi(\phi_{[IJKL]})}{\partial r^{\beta}_{J}} + r^{\alpha}_{K}\frac{\partial U_\phi(\phi_{[IJKL]})}{\partial r^{\beta}_{K}} + r^{\alpha}_{L}\frac{\partial U_\phi(\phi_{[IJKL]})}{\partial r^{\beta}_{L}}\right\},$$

where Ω is a volume. When calculating the overall macrostresses $\Sigma^{zz}_{overall}$, Ω is taken to be the volume of the entire simulation box. For calculating micro or local stresses, Ω is taken to be the volume of a subset of the entire box [29]. Long range corrections are used to calculate the stress tensors. Also shown in Fig. 6 is the overall macrostress carried by the sample, which is calculated based on the entire volume. The dashed curve is a measure of microstress computed using a volume that lies entirely in the voided region (shown circled in inset) while the dash-dotted curve is based on a volume that lies entirely in the bulk. The latter curve does not show any hardening while the former hardens steeply. The hardening is entirely attributable to the presence of end anchored chains that are devoid of entanglements in the middle and can stretch in a manner akin to rubber molecules. The macrostress, which is the average of all the microstresses, follows the dash-dotted curve closely. It should however, be noted that though the overall response does not exhibit hardening, there are steeply hardening regions embedded in the material.

V. CONCLUSIONS

We have investigated the role of deformation induced disentanglement in the first stages of void nucleation in glassy polymers. The following important facts have come to light from this investigation:

(1) Under highly triaxial states of stress, deformation induced disentanglement has an important role to play in the nucleation of voids in glassy polymers.

(2) The distinction between topological entanglements (which are binary contacts between chains) and rheological entanglements assume importance in this context. Deforma-

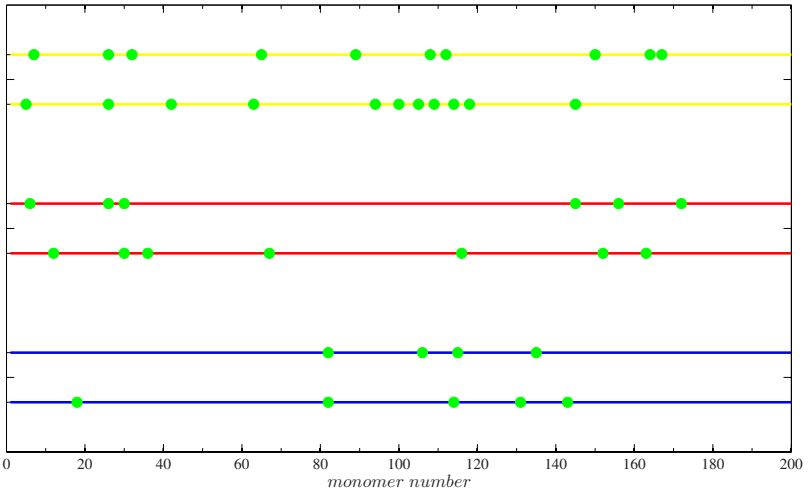

FIG. 5. (Color online) The location of entanglement points are marked by solid circles on the three chains marked yellow, red and blue in Fig. 3. The position of entanglement points are shown at $\lambda=1.0$ and $\lambda=2.0$ for each chain.

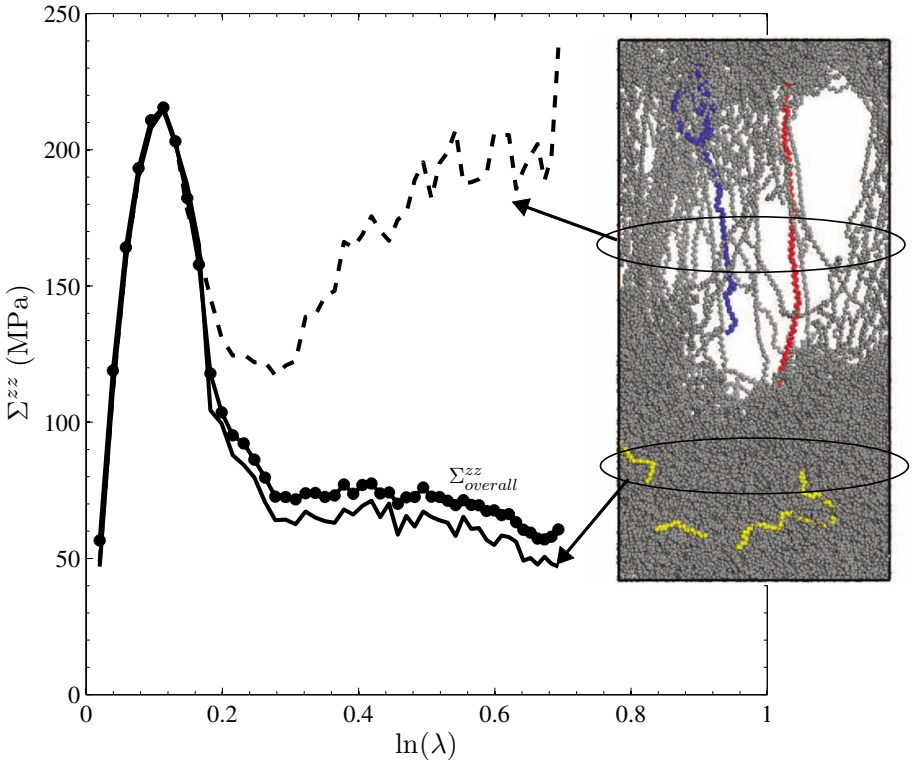

FIG. 6. (Color online) The stress carried by the whole and two different sub region of the simulation box in Fig. 3 plotted against the logarithmic stretch $\ln(\lambda)$.

tion (at least up to the stages that have been simulated here, i.e., $\lambda=2$) seems to reduce the number of rheological entanglements keeping the number of topological entanglements constant.

(3) While loss and rearrangement of topological entanglements take place throughout the ensemble, at certain "favorable" locations the rearrangement is dramatic. Such rearrangements leave long portions of a number of chains free of entanglements while all topological entanglements move to their ends, anchoring them firmly.

(4) Thus "voided" regions are created from which all chains have slipped away except a few that are firmly anchored at the ends and pulled taut. On further deformation, even these chains might either break or pull out from the bulk enabling the void to expand even more easily.

(5) The taut chains carry a large stress especially at large strains. On the contrary, chains in the bulk do not harden.

Two immediate consequences of our results merit mention here. First, constitutive models for glassy polymers are often formulated on the premise that a glassy polymer is a network of macromolecular chains embedded in an elastoviscoplastic matrix and at large levels of deformation, significant stress carrying capacity is derived from the stretching of the network. The network is formed of chain strands held together at fixed entanglement points and the prospect of loss or slippage of entanglements is not generally considered. Our results show that even in the glassy state, the entanglement network evolves with deformation and realistic constitutive models need to account for the dissipation due to slippage of chains and loss of entanglements and/or scission of chains.

Second, cavitation criteria are frequently formulated in terms of the state of stress, particularly the mean stress. Our results point to the fact that cavitation in glassy amorphous polymers may be additionally related to the entanglement length, scission strength etc. of the macromolecule being studied thus yielding a more polymer-specific cavitation criterion.

ACKNOWLEDGMENT

One of the authors (D.K.M.) wishes to thank the Indo-French Centre for the Promotion of Advanced Research for providing support for this work under project No. 3608-1. The authors also wish to express their gratitude to Professor Martin Kröger from ETH Zurich for sharing the Z1 code.

[1] S. S. Sternstein and L. Ongchin, Polym. Prepr. (Am. Chem. Soc. Div. Polym. Chem.) **10**, 1117 (1969).
[2] E. J. Kramer, Adv. Polym. Sci. **52-53**, 1 (1983).
[3] A. S. Argon, Philos. Mag. **36**, 1195 (1977).
[4] A. N. Gent, J. Mater. Sci. **5**, 925 (1970).
[5] M. Dettenmaier and H. H. Kausch, Colloid Polym. Sci. **259**, 937 (1981).
[6] M. Dettenmaier, Adv. Polym. Sci. **52-53**, 57 (1981).
[7] E. J. Kramer and L. L. Berger, Adv. Polym. Sci. **91-92**, 1 (1990).
[8] S. K. Sukumaran, G. S. Grest, K. Kremer, and R. Everaers, J. Polym. Sci., Part B: Polym. Phys. **43**, 917 (2005).

[9] M. Kröger, Comput. Phys. Commun. **168**, 209 (2005).
[10] R. S. Hoy, K. Foteinopoulou, and M. Kröger, Phys. Rev. E **80**, 031803 (2009).
[11] C. Tzoumanekas and D. N. Theodorou, Macromolecules **39**, 4592 (2006).
[12] D. K. Mahajan and S. Basu, Modell. Simul. Mater. Sci. Eng. **18**, 025001 (2010).
[13] D. K. Mahajan and S. Basu, Int. J. App. Mech. **1**, 1 (2010).
[14] M. Fukuda and S. Kuwajima, J. Chem. Phys. **107**, 2149 (1997).
[15] D. Brown and J. H. R. Clarke, Macromolecules **24**, 2075 (1991).
[16] I. Ogura and T. Yamamoto, Polymer **36**, 1375 (1995).
[17] K. Yashiro, T. Ito, and Y. Tomita, Int. J. Mech. Sci. **45**, 1863 (2003).
[18] W. Tschöp, K. Kremer, J. Batoulis, T. Burger, and O. Hahn, Acta Polym. **49**, 61 (1998).
[19] W. Tschöp, K. Kremer, O. Hahn, J. Batoulis, and T. Burger, Acta Polym. **49**, 75 (1998).
[20] Q. Sun and R. Faller, Comput. Chem. Eng. **29**, 2380 (2005).
[21] M. K. Majumder, R. S., D. K. Mahajan, and S. Basu, Phys. Rev. E **81**, 011803 (2010).
[22] R. Auhl, R. Everarers, G. S. Grest, K. Kremer, and S. J. Plimpton, J. Chem. Phys. **119**, 12718 (2003).
[23] O. Alexiadis, V. G. Mavrantzas, R. Khare, J. Beckers, and A. R. C. Baljon, Macromolecules **41**, 987 (2008).
[24] B. Wunderlich, J. Chem. Phys. **37**, 1207 (1962).
[25] R. Everaers, S. K. Sukumaran, G. S. Grest, C. Svaneborg, A. Sivasubramanian, and K. Kremer, Science **303**, 823 (2004).
[26] S. Shanbhag and R. G. Larson, Macromolecules **39**, 2413 (2006).
[27] K. Foteinopoulou, N. C. Karayiannis, V. G. Mavrantzas, and M. Kröger, Macromolecules **39**, 4207 (2006).
[28] A. F. Terzis, D. N. Theodorou, and A. Stroeks, Macromolecules **35**, 508 (2002).
[29] W. Chen and J. Fish, Int. J. Numer. Methods Eng. **67**, 189 (2006).